Precise Relative Navigation in Medium Earth Orbits with Global Navigation Satellite Systems and Intersatellite Links for Black Hole Imaging

Salas, María; Fernández, Jaime; van den IJssel, Jose

DOI
10.1016/j.asr.2023.10.037

Publication date
2024

Document Version
Final published version

Published in
Advances in Space Research

Available online at www.sciencedirect.com

ScienceDirect

Advances in Space Research 74 (2024) 2599–2614

ADVANCES IN SPACE RESEARCH (a COSPAR publication)

www.elsevier.com/locate/asr

Precise Relative Navigation in Medium Earth Orbits with Global Navigation Satellite Systems and Intersatellite Links for Black Hole Imaging

María Salas [a,b], Jaime Fernández [b], Jose van den IJssel [a]

[a] Delft University of Technology, Mekelweg 5 2628 CD, Delft, the Netherlands
[b] GMV AD., Isaac Newton 11 28760, Tres Cantos, Spain

Received 30 June 2023; received in revised form 20 October 2023; accepted 23 October 2023
Available online 31 October 2023

Abstract

The Event Horizon Telescope (EHT) is a ground-based array of Very Long Baseline Interferometry (VLBI) telescopes designed to image the event horizon of black holes. To overcome its limitations, this study explores a mission concept involving a two-satellite constellation of VLBI telescopes deployed in Medium Earth Orbit (MEO). Achieving high-resolution black hole images requires precise baseline determination at the millimetre level. To address this challenge, each satellite in the constellation is equipped with two Global Navigation Satellite System (GNSS) receivers and an optical Intersatellite Link (ISL) to enhance orbit determination. The results highlight the importance of integer ambiguity resolution and reveal that the ISL primarily improves baseline estimation along the link direction, with minimal impact along the black hole direction. Large intersatellite distances lead to sub-optimal relative orbit accuracy, challenging the attainment of the 3.5 mm relative position accuracy goal along the black hole direction.

Keywords: Precise Orbit Determination; POD; Relative Navigation; GNSS; Intersatellite Links; VLBI

1. Introduction

The Event Horizon Telescope (EHT) is a global Very Long Baseline Interferometry (VLBI) array consisting of ground-based telescopes specifically designed for imaging the event horizon of black holes. Among its primary targets are Sagittarius A* (Sgr A*), located at the centre of our galaxy, and the black hole situated at the core of the Messier 87 galaxy, known as M87* (Akiyama et al., 2019). Fig. 1 showcases an image of M87* captured by the EHT.

The performance of the EHT system is limited by various factors, including atmospheric effects, sparse coverage of the sky, and restricted angular resolution. Particularly, the angular resolution is constrained by the baseline distance between telescopes, which is inherently limited by the Earth's diameter. To overcome these challenges, one potential solution being explored is the deployment of VLBI telescopes in space (Kudriashov et al., 2021).

For this purpose, the European Space Agency (ESA) has proposed a mission concept involving a constellation of two space-born telescopes deployed in Medium Earth Orbits (MEO) known as the Event Horizon Imager (EHI) constellation. The successful development of this space VLBI system depends on achieving a very precise baseline determination between the two spacecraft (Kudriashov et al., 2021). The mission will track the black hole in three frequencies: 3 GHz, 230 GHz, and 557 GHz, with wavelengths of 7, 1.3, 0.54 mm respectively. In principle, it is enough to correlate the VLBI observation with the

E-mail addresses: m.salas.lasala@gmail.com (M. Salas), jfernandez@gmv.com (J. Fernández), j.a.a.vandenijssel@tudelft.nl (J. van den IJssel)

https://doi.org/10.1016/j.asr.2023.10.037
0273-1177/

Fig. 1. An image of the black hole at the center of galaxy M87 (Credits: Event Horizon Telescope collaboration).

longest wavelength (7 mm) to allow subsequent VLBI observation correlation with wavelength bootstrapping (Boer & Brinkerink, 2023). Specifically, a 3-dimensional relative position accuracy of 3.5 mm (3-sigma) is required during post-processing (i.e., half of the longest wavelength used). Meeting this stringent relative navigation requirement is crucial, especially in the direction aimed at the black hole, as the attainment of high-quality black hole images heavily relies on fulfilling this demand (GMV, 2022). The EHI satellites are equipped with Global Navigation Satellite Systems (GNSS) receivers and an Intersatellite Link (ISL) to accomplish this navigation objective.

While precise orbit determination traditionally relies on GNSS observations, recent years have witnessed a growing utilization of intersatellite links in the field. ISLs serve various purposes, from facilitating data communication to enabling precise ranging between satellites. Notable missions, including GRACE (Gravity Recovery And Climate Experiment), GRACE Follow-On, and BeiDou-3, have already embraced ISL technology to enhance orbit determination and satellite synchronization (Kornfeld et al., 2019; Zhu et al., 2022).

Looking ahead to future missions, ISL technology is set to play a pivotal role. Upcoming missions, such as LISA (Laser Interferometer Space Antenna) and the Kepler system concept, which is under consideration for integration into a future generation of Galileo, are planning to incorporate optical intersatellite links (Amaro-Seoane et al., 2019; Michalak et al., 2021). Consequently, ISLs emerge as a crucial component in modern and future satellite constellations to enhance their overall performance.

The EHI constellation consists of two spacecraft, EHI-1 and EHI-2, located in coplanar polar orbits at altitudes of 8,280 km and 8,303.3 km, respectively. Both satellites have a Right Ascension of the Ascending Node (RAAN) of 140.9 deg, ensuring an optimal orbital plane for imaging both Sgr A* and M87*. Initially, the EHI satellites will be separated by 23.3 km, which will gradually increase over time due to the difference in their orbital period. The relative geometry between the EHI orbits exhibits an 86-day cycle, with approximately 30 days of ISL visibility. This results in a varying baseline ranging from 23.3 km to approximately 25,000 km, highlighting the high-dynamic baseline nature of the EHI constellation. Although the mission aims to image both black holes, this study focuses specifically on Sgr A*. Consequently, the attitude law governing the satellites is designed to continuously point towards Sgr A*, whose inertial position is fixed in space (GMV, 2022).

Each EHI satellite is equipped with a range of sensors, including two GNSS antennas, an ISL instrument, a VLBI antenna, star trackers, and a master clock. The GNSS configuration involves two hemispherical antennas for GPS and Galileo tracking that are positioned on opposite sides of the spacecraft to maximize visibility. One of the antennas (Q2) is oriented towards the target black hole, while the other antenna (Q1) points in the opposite direction. Moreover, the ISL sensor consists of a two-way optical link employing a Nd-YAG laser operating at a wavelength of 1064 nm (GMV, 2022). Fig. 2 depicts the geometry of the EHI spacecraft, highlighting the location of the GNSS and ISL sensors.

The main objective of this study is to explore the feasibility of achieving very precise relative positioning between the two EHI satellites to enable accurate black hole imaging. The goal is to assess the level of relative accuracy attainable through a stand-alone approach during post-processing. By undertaking this investigation, the study aims to identify and address the limitations and challenges associated with achieving high-precision relative navigation within high-dynamic MEO constellations.

2. Methodology

A detailed simulation study is performed using the software package ***FocusPOD,*** which is powered by the C++ flight dynamics library **GMV MAORI** (Multi-purpose Advanced Orbit Restitution Infrastructure) developed by GMV (Fernández Martín et al., 2023). This is the software that is used in this study to simulate the observational data, as well as to perform the orbit determination process.

2.1. Generation of reference orbits

As the EHI mission has not been launched, there is no real data available. Therefore, the orbits of both the GNSS and EHI satellites must be simulated to generate the observations. The reference orbits of 30 GPS and 24 Galileo satellites are generated using the dynamical model presented in Table 1. In addition, this table also shows the more complex dynamical model employed to generate the reference orbits of EHI-1 and EHI-2. Atmospheric effects

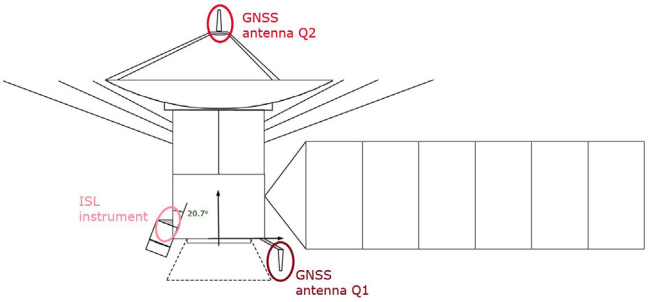

Fig. 2. EHI spacecraft configuration (GMV, 2022).

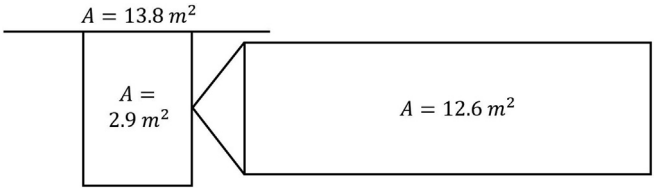

Fig. 3. Simplified macro-model of the EHI satellite.

are not considered in the propagation because they are not relevant at the altitude of the EHIs (Montenbruck & Gill, 2000). These reference orbits are considered the representation of reality. In all propagations, a multi-step 8th Adams-Bashforth-Moulton propagator is used (Montenbruck & Gill, 2000), with 420 steps per revolution.

To simulate the effects of solar and Earth radiation on the EHI satellites, the box-wing macro-model depicted in Fig. 3 has been employed. This macro-model is a simplified version of the model presented in Fig. 2. In this simplified model, the satellite's geometry is divided into three main parts: the body, the solar panel (SP), and the VLBI antenna. The areas of this simplified macro-model are compiled in Table 2. The VLBI antenna is represented by the X panels, while the lateral areas of the main body are represented by the Y and Z panels. Furthermore, Table 2 provides a summary of the spacecraft's optical properties, which include the visible specular reflectance ($\rho_{s,VIS}$), visible diffuse reflectance ($\rho_{d,VIS}$), visible absorptance (α_{VIS}), infrared specular reflectance ($\rho_{s,IR}$), infrared diffuse reflectance ($\rho_{d,IR}$), infrared absorptance (α_{IR}), and whether re-radiation is taken into consideration.

2.2. Generation of reference clocks

In a similar manner to the ephemeris data, it is necessary to simulate the GNSS and EHI clocks to generate the observations. The model described by Galleani et al. (2003) is used to simulate the clocks. This model requires the consideration of several clock parameters, including the clock diffusion coefficients of the phase deviation (σ_1) and the 'random walk' component of the frequency deviation (σ_2). These two parameters are adjusted for each clock by analysing real clocks used in GNSS navigation and matching their Allan deviation.

The final clock products from the Center of Orbit Determination in Europe (CODE) are employed to analyse the GNSS clocks. The data used has a sampling rate of 5 s and corresponds to the period between 01/01/2023 and 24/01/2023. Fig. 4 presents the Allan deviation of one clock from each operational GPS block, along with the simulated clock that was found to be the best match. Similarly, the Allan deviation of Galileo clocks is shown in Fig. 5, as well as the simulated clock that was found to be the best match for Galileo. In contrast to GPS, σ_2 is lower because Galileo clocks appear to exhibit a better long-term stability.

In contrast, the clocks of Sentinel-3A, −3B, and −6A estimated by GMV's Copernicus Precise Orbit Determination (CPOD) operational service are used to generate the EHI clocks. The clock data has a sampling rate of 10 s and corresponds to the period from 31/12/2022 20:00:00 to 02/01/2023 04:00:00. Fig. 6 presents the Allan deviation of the Sentinel-3A (S3-A), Sentinel-3B (S3-B), and Sentinel-6A (S6-A) clocks. The simulated clock that best matched the stability of these ultra-stable oscillators is also shown in the figure.

A summary of the parameters used for simulating all the required clocks can be found in Table 3. Notice that other clock model parameters, such as the initial bias (b_0), initial drift (d_0) and frequency drift (Δf), have been set zero for simplicity.

Table 1
Dynamical model of GNSS and EHI reference orbits.

Contribution	GNSS	EHI-1 & EHI-2
Gravity Field (static)	COST-G (12x12) (Jäggi et al., 2020)	COST-G (35x35)
Gravity Field (time-varying)	Drift/annual/semi-annual piece-wise terms (1x1)	Drift/annual/semi-annual piece-wise terms (10x10)
Solid Earth Tides	IERS 2010 (Petit & Luzum, 2010)	IERS 2010
Ocean Earth Tides	FES2014 (12x12) (Lyard et al., 2021)	FES2014 (35x35)
Earth Pole Tides	IERS 2010	IERS 2010
Ocean Pole Tides	IERS 2010	IERS 2010
Third Body	Sun, Moon, Planets DE405 (Standish, 1998)	Sun, Moon, Planets DE405
Relativistic Gravitation	IERS 2010	IERS 2010
Solar Radiation Pressure	Constant area	Macro-model
Earth's Albedo	Not applied	Macro-model
Earth's Infra-red	Not applied	Macro-model
Atmospheric Effects	Not applied	Not applied
Attitude Law	GPS/Galileo	Sgr A* pointing law

Table 2
Areas and surface optical properties of the EHI simplified macro-model.

Panel	Area [m^2]	$\rho_{s,VIS}$	$\rho_{d,VIS}$	α_{VIS}	$\rho_{s,IR}$	$\rho_{d,IR}$	α_{IR}	Re-radiation
+X, -X	13.8	0.6000	0.0500	0.3500	0.1900	0.2000	0.6100	Yes
+Y	2.9	0.2312	0.3362	0.4326	0.1462	0.1016	0.7522	Yes
-Y	2.9	0.2096	0.0446	0.7458	0.2213	0.0661	0.7126	Yes
+Z	2.9	0.4205	0.0450	0.5245	0.13764	0.20646	0.6559	Yes
-Z	2.9	0.3570	0.0730	0.5700	0.1920	0.1910	0.6170	Yes
SP front	12.6	0.0900	0.0	0.9100	0.1900	0.0	0.8100	No
SP back	12.6	0.0800	0.0	0.9200	0.0	0.1809	0.8200	No

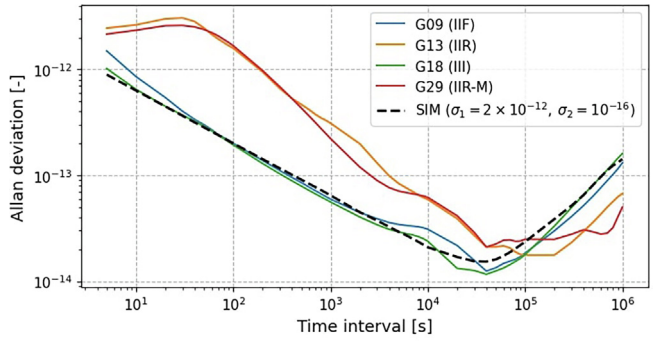

Fig. 4. Allan deviation of real GPS clocks and the optimal simulated GPS clocks.

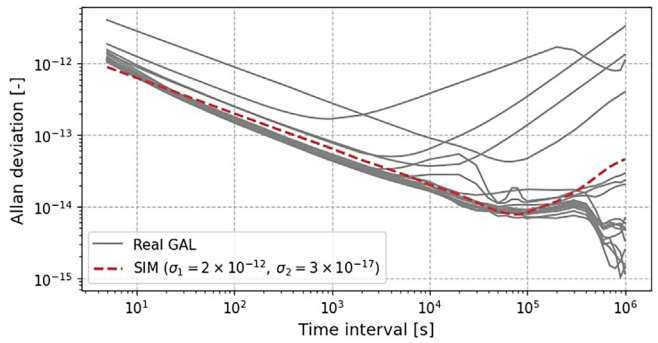

Fig. 5. Allan deviation of real Galileo clocks and the optimal simulated Galileo clocks. Each grey line represents a different clock within the constellation.

Table 3
Parameters used to simulate the GNSS and EHI clocks.

Parameter	GPS	GAL	EHI-1 & −2
$\sigma_1[-]$	2×10^{-12}	2×10^{-12}	2×10^{-11}
$\sigma_2[-]$	1×10^{-16}	3×10^{-17}	5×10^{-16}

2.3. Generation of GNSS observations

Dual-frequency pseudo-range and carrier-phase GNSS observations are simulated at a rate of 10 s. The receiver tracks GPS signals in L1 and L5 frequencies, and Galileo signals in E1 and E5a. To simulate the visibility between the GNSS and EHI satellites, the field-of-view (FOV) semi-angle is assumed to be 23.5 deg for GPS and 20.5 deg for Galileo. In contrast, the EHI antennas have an aperture of 180 deg, allowing the EHIs to see the whole sky. With these GNSS´s FOV, the tracking is done only on the main lobe, excluding tracking from the unknown secondary lobes.

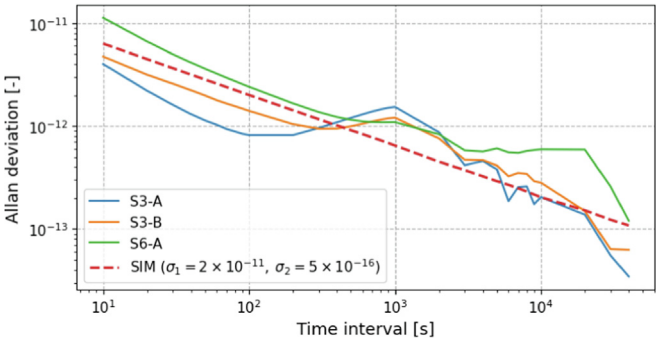

Fig. 6. Allan deviation of Sentinel-3A, −3B and −6A clocks and the optimal simulated EHI clock.

The simulation of the GNSS observable involves accounting for various contributions, including the geometric range, relativistic range, emitter and receiver clock offsets, location of the antenna reference point, antenna phase centre offset, antenna phase centre variations, phase wind-up, and phase ambiguity. The phase ambiguity is simulated as a pass-wise random integer number of cycles without cycle slips.

Due to the high orbital regime, most of the GNSS observables will not be perturbed by the ionosphere, and therefore this was not included in the simulation of the GNSS observations. In any case, dual-frequency observations are combined to create the ionospheric-free observable, which it is known that eliminates 99% of the ionospheric delay (Teunissen & Montenbruck, 2017) on real observations, at the cost of increasing the noise of the observables. Moreover, a grazing altitude of 100 km is set to filter out signals affected by the troposphere without compromising visibility.

Regarding multipath effects, it should be noted that they can be of significance for the current satellite design, particularly due to the positioning of the GNSS antenna Q2. As depicted in Fig. 2, this antenna is mounted on the feed of a large parabolic antenna. This specific configuration intro-

duces the potential for substantial multipath noise, which could be both significant in magnitude and temporally correlated. It is important to acknowledge that realistically modelling this multipath effect presents a major challenge, that it is coupled with the design of the satellite, the parabolic antenna and the GNSS antenna. In this study, the explicit modelling of multipath effects has been neglected, with the assumption that their impact may be mitigated through a clever design that minimizes the multipath, and a proper characterization of the phase-centre offset and variations, particularly when considering the static nature of the parabolic antenna and the solar panel.

Furthermore, thermal noise and instrumental delays are introduced into the GNSS observations. The thermal noise at the GNSS receiver affects the quality of the observations. To model this noise, Kaplan & Hegarty (2006) propose a Gaussian noise model that considers the signal-to-noise ratio of the signal. The standard deviations for the code and phase observables are computed using Eqs. (1) and (2), respectively.

$$\sigma_{PR} = \lambda_C \sqrt{\frac{Bd}{2C/N_0}\left(1 + \frac{1}{T_c C/N_0}\right)} \tag{1}$$

$$\sigma_{CP} = \frac{\lambda}{2\pi}\sqrt{\frac{Bd}{C/N_0}\left(1 + \frac{1}{2T_c C/N_0}\right)} \tag{2}$$

where λ_C is the signal chip length, B is the loop noise bandwidth, d is the correlation spacing, T_c is the coherent integration time, λ is the signal wavelength, and C/N_0 is the carrier-to-noise ratio.

The parameters in Equation (1) and (2) vary depending on the frequency band of the transmitted signal. Table 4 and Table 5 summarize the values corresponding to GPS L1 and L5, and Galileo E1 and E5a code and phase observations, based on the parameter values proposed by Zangerl (2017) for a LEO POD receiver.

The simulation of the carrier-to-noise ratio takes into account the transmitter antenna Gain and power, the receiver antenna Gain, the system noise temperature, and the free-space path losses according to the link budget model presented by Perello-Gisbert & Garcia (2010). In this simulation, the hardware losses are set to zero. To maintain the quality of the GNSS observations, any observations with a signal-to-noise ratio lower than 30 dB are filtered out.

Table 4
Code tracking loop parameters.

Parameter	Code L1	Code E1	Code L5/E5a
Loop bandwidth, B [Hz]	0.5	0.5	0.25
Coherent integration time, T_c [ms]	10	12	20
Correlation spacing, d [chips]	0.1412	0.0706	0.706
Chip length, λ_C [m]	293.05	293.05	29.305

Table 5
Carrier tracking loop parameters.

Parameter	Carrier L1	Carrier E1	Carrier L5/E5a
Loop bandwidth, B [Hz]	10	10	5
Coherent integration time, T_c [ms]	10	12	20
Wavelength, λ [mm]	190.29	190.29	254.8

Modelling the instrumental delays is also essential in high-precision orbit determination applications, especially when using integer ambiguity resolution. Different analysis centres, like CODE, provide the instrumental biases of the GNSS satellites. These centres provide estimated values of the bias parameters and their corresponding estimated standard deviations. The typical distribution of the bias final products provided by CODE was analysed to simulate these biases. It was observed that code biases were uniformly distributed between −15 m and 15 m, while phase biases were between −1.5 mm and 1.5 mm. Therefore, GNSS and receiver code and phase biases are then randomly generated according to this uniform distribution. However, the GNSS code biases are set to zero since the simulation of the GNSS clocks and biases is not coupled, and introducing code biases would not be consistent with this decoupled model.

2.4. Generation of ISL observations

The ISL observable is modelled as a very high-frequency pseudo-range observation. To simulate the visibility of this link, it is assumed that the ISL instruments have a 360 deg FOV, ensuring continuous line-of-sight visibility between the EHI satellite. This FOV is a requirement of the mission to allow real-time correlation of the VLBI observations. The simulated ISL observations are generated at a rate of 10 s and include the geometrical range, relativistic effects, and location of the ISL instrument reference point. Since the ISL measurements are two-way, it is not required to include clock offsets (Alawieh et al., 2016). Similar to the GNSS observations, a grazing altitude of 100 km is used to avoid the troposphere. Moreover, the frequency of the optical ISL is high enough so that it is not affected by the ionosphere above 100 km (Loscher, 2010).

Due to the lack of detailed information about the ISL instrument characteristics, it is difficult to develop an accurate model of laser error sources related to frequency instability, satellite vibrations, tracking errors, and background noise. As a result, these effects are modelled as random white Gaussian noise with a standard deviation similar to state-of-the-art optical ISL precision, which is 1 mm in the worst-case scenario (Giorgi et al., 2019; Michalak et al., 2020; Michalak et al., 2021).

Moreover, it is important to note that hardware delays associated with the ISL instrument are not considered in the simulation. This implies that the results obtained when considering the ISL should be viewed as optimistic. In this study, this simplified modelling approach of the ISL observations is adopted in order to provide initial insights into

the potential of this technology without delving into the complexities of the instrument. While acknowledging that a comprehensive model of ISL biases and noise characteristics, as well as its integration into the POD process, is missing, the simplification employed here is sufficient for highlighting the pros and cons of ISL for achieving the goal of this particular mission, i.e., relative navigation in the direction of the black hole.

2.5. Error sources

To obtain realistic simulation results, several sources of uncertainty are included in the Precise Orbit Determination (POD) process. These sources include perturbing the GNSS orbits and clocks used in the POD, perturbing the GNSS instrumental biases used in the POD, and using a different geopotential model and solar radiation pressure model to those used in the simulation of the reference orbits.

2.5.1. Errors in the GNSS orbits and clocks

In real-world scenarios, the precise orbits and clocks of GNSS satellites are not simulated, but rather provided by the International GNSS Service (IGS) analysis centres. Although IGS products are highly precise, they are not completely free from errors. As such, to conduct realistic simulations, it is important to model the errors present in these orbits and clocks. The GNSS ephemerides contain systematic once-per-revolution errors that result mainly from unmodeled forces. These errors tend to be harmonics of the orbital period in the radial, along-track, and cross-track orbital directions (Urschl et al., 2007). The position error in each direction of the orbital QSW frame is described by Eq. (3). The QSW frame is based on the satellite orbit, with the Q axis aligned with the radial direction, the S axis aligned with the along-track direction, and the W axis aligned with the cross-track direction.

$$\Delta r_i(t) = A_i \cos\left(2\pi \frac{t - t_0}{T} + \varphi_i\right), i = \{Q, S, W\} \tag{3}$$

where $\Delta r_i(t)$ is the error generated at time t, t_0 is the initial time, T is the orbital period, A is the amplitude error, and φ is the phase error. The amplitude and phase errors are random variables normally distributed according to $A \sim N(0, \sigma_A)$ and $\varphi \sim N(0, 2\pi)$.

GNSS clock errors are correlated with orbit errors due to the coupling of the clock estimation with the radial component of position. Thus, GNSS clock errors also exhibit a harmonic behaviour associated with radial position errors (Senior et al., 2008). Furthermore, clock errors display a time-correlated behaviour (Olynik et al., 2002). As a consequence, clock errors can be modelled as a combination of an orbit-related component and a Gauss–Markov process. In particular, the Gauss–Markov clock error is computed according to Eq. (4).

$$\Delta\delta_{GM}(t_k) = \Delta\delta_{GM}(t_{k-1}) e^{(t_{k-1}-t_k)/\tau} + \sqrt{1 - e^{2(t_{k-1}-t_k)/\tau}}\, w(t_k) \tag{4}$$

where $\Delta\delta_{GM}(t_k)$ is the Gauss–Markov clock error being generated, t_k and t_{k-1} are two consecutive epochs, τ is the correlation time of the process, and w is the uncorrelated random noise that follows the normal distribution $w \sim N(0, \sigma_w)$.

The model provides several degrees of freedom to characterize the GNSS orbit and clock errors, namely σ_A, σ_w and τ. These parameters must be carefully selected to introduce realistic errors into the analysis. To achieve this, the orbit and clock products from two analysis centres, CODE and GFZ (German Research Centre for Geosciences), have been compared to gain insights into the order of magnitude and time behaviour of these errors. The comparison between the final GPS orbit and clock products provided by CODE and GFZ on 08/01/2023 are shown in Fig. 7 (left). The orbit comparison is projected along the radial, along-track and cross-track directions. The behaviour of the comparison of the Galileo products is similar to the one for GPS.

Subsequently, the parameters of the model were adjusted to ensure that the comparison between the reference and perturbed orbits and clocks closely aligns with the comparisons between the different analysis centres. Based on this analysis, the values chosen for these parameters are $\sigma_A = 2$ cm, $\sigma_w = 70$ ps, and $\tau = 30$ min. Fig. 7 (right) depicts the comparison between the reference GPS products and the perturbed GPS products using these adjusted parameters.

2.5.2. Uncertainties in the GNSS instrumental delays

To introduce GNSS instrumental bias uncertainty in the POD process, perturbations are added to these biases. The perturbations follow a normal distribution, with mean equal to the previously simulated bias value and a random standard deviation. For GNSS code instrumental biases, this standard deviation follows a normal distribution $N \sim (0.02, 0.001)$ ns. These values were determined by analysing the standard deviation of code biases provided by CODE.

As for the GNSS phase biases, it was observed that their standard deviations were always set to zero in the CODE bias files. Nonetheless, it was decided to perturb these biases to explore the potential impact of uncertainty in the emitter phase biases on the POD process. After conducting various experiments, it was determined that the standard deviation of the GNSS phase biases should follow a normal distribution $N \sim \left(10^{-4}, 10^{-5}\right)$ ns.

2.5.3. Uncertainties in the geopotential model

Realistic gravity field model errors are introduced by using two different geopotential models. The COST-G (Combination Service for Time-variable Gravity fields) model is employed in the generation of the reference orbits

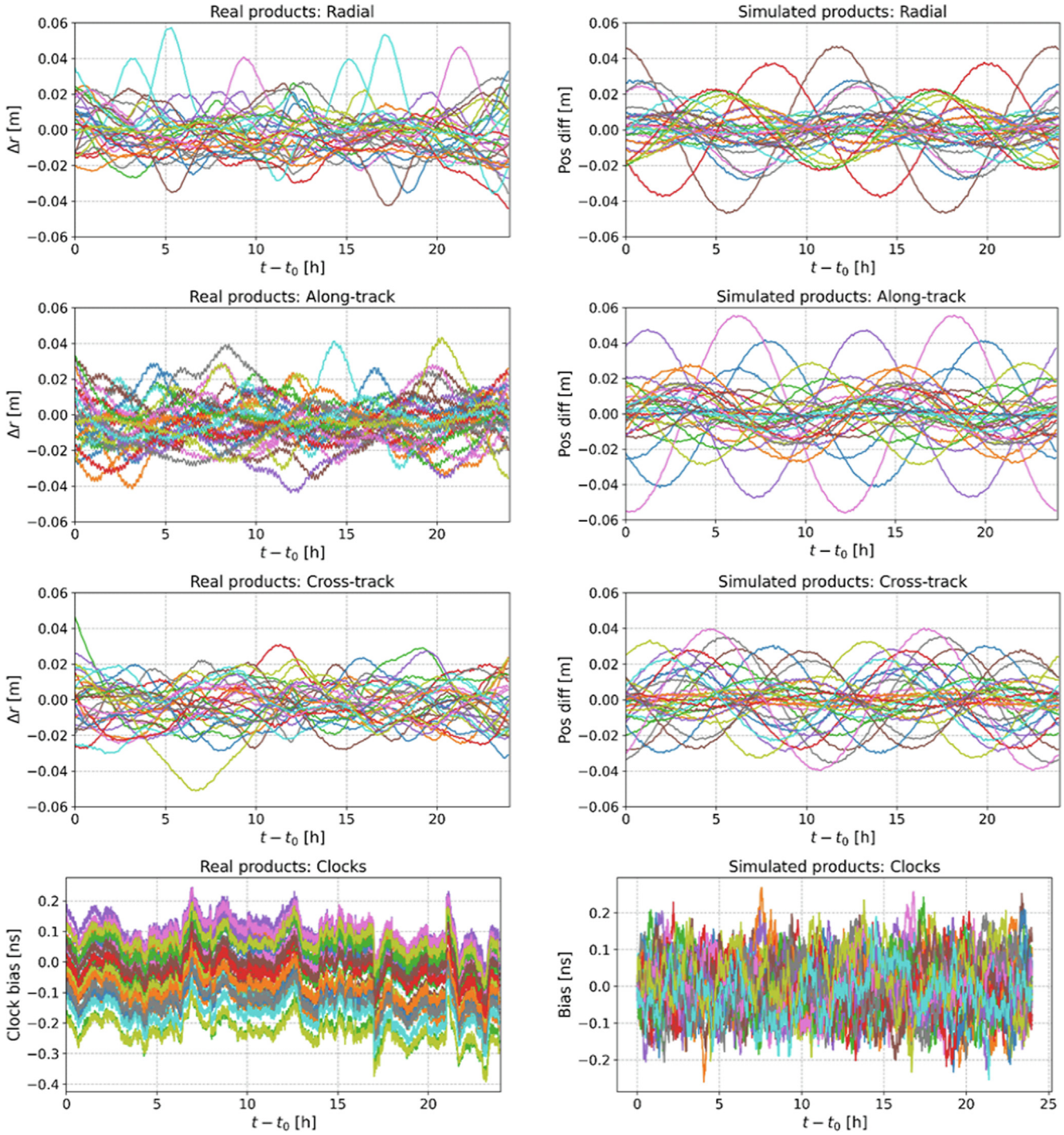

Fig. 7. Comparison between CODE and GFZ final GPS orbit and clock products on 08/01/2023 (left) and comparison between the reference GPS orbits and clocks and the perturbed GPS orbits and clocks (right). Each line represents a different GPS satellite.

and simulation of the observations, while the EIGEN.GRGS.RL04.MEAN-FIELD.quadratic_mean_pole (European Improved Gravity model of the Earth by New techniques) model is used in the orbit determination process.

The difference between these two geopotential models becomes larger as time progresses. The increasing discrepancies between the geopotentials are due to the fact that the COST-G model is regularly updated every four months, incorporating time-dependent terms, whereas the EIGEN model has not changed since 2019 (Berzosa et al., 2023). Therefore, the year 2022 is selected for the simulations to introduce a considerable level of uncertainty into the orbit determination process.

2.5.4. Uncertainties in the SRP model

Two distinct solar radiation pressure (SRP) models are also employed during the simulation and estimations stages. An analytical box-wing model is used in the simula-

tion, and a modified empirical ECOM (Empirical CODE Orbit Model) model in the POD estimation.

The standard ECOM model decomposes the perturbing SRP acceleration into three orthogonal directions that are well-adapted to SRP modelling (Arnold et al., 2015). The D axis is in the direction satellite-Sun, Y is perpendicular to the plane satellite-Sun-Earth, and B completes the right-handed orthogonal reference system, as illustrated in Fig. 8. The Y direction aligns with the solar panel axis if the satellite follows a yaw-steering attitude law.

The total SRP acceleration is decomposed in these three axes and a set of empirical coefficients is estimated. In the original ECOM, these coefficients are expressed according to Eq. (5), where u is the satellite's argument of latitude.

$$\begin{aligned} D(u) &= D_0 + D_c cos(u) + D_s sin(u) \\ Y(u) &= Y_0 + Y_c cos(u) + Y_s sin(u) \\ B(u) &= B_0 + B_c cos(u) + B_s sin(u) \end{aligned} \quad 5$$

$$\begin{aligned} Y(u) &= Y_0 + Y_c cos(u) + Y_s sin(u)\, B(u) \\ &= B_0 + B_c cos(u) + B_s sin(u) \end{aligned}$$

This model is specifically designed for satellites that follow a yaw-steering attitude law, where the Y axis aligns with the solar panels. Hence, it cannot be expected to accurately represent the behaviour of satellites following different attitude laws (Prange et al., 2017). To address this issue for satellites following an orbit-normal (ON) attitude law, Prange et al. (2020) redefined the Y and B axes of the standard ECOM model to better capture the influence of the attitude of the satellite.

The EHI spacecraft deviate from both the yaw-steering and orbital-normal attitude laws and instead follow an inertial attitude law, aligning themselves with the black hole Sgr A*. The ON mode adaptation served as inspiration to develop a modified ECOM system suitable for the EHI attitude law. In this modified frame, referred to as ECOM-SGRA, the D axis remains aligned with the satellite-Sun direction. The Y axis is redefined as perpendicular to both D and the direction pointing towards the black hole, while the B axis completes the orthogonal frame. Eq. (6) shows the mathematical definition of the ECOM-SGRA axes. This is the SRP model used in the POD.

$$\widehat{\boldsymbol{D}} = \frac{\boldsymbol{r}_\odot - \boldsymbol{r}}{|\boldsymbol{r}_\odot - \boldsymbol{r}|}, \widehat{\boldsymbol{Y}} = \widehat{\boldsymbol{D}} \times \frac{\boldsymbol{r}_{SGRA}}{|\boldsymbol{r}_{SGRA}|}, \widehat{\boldsymbol{B}} = \widehat{\boldsymbol{D}} \times \widehat{\boldsymbol{Y}} \quad (6)$$

where $\boldsymbol{r}_\odot, \boldsymbol{r}$ and $\boldsymbol{r}_{SGRA}$ are the inertial position of the Sun, the satellite, and Sgr A*, respectively.

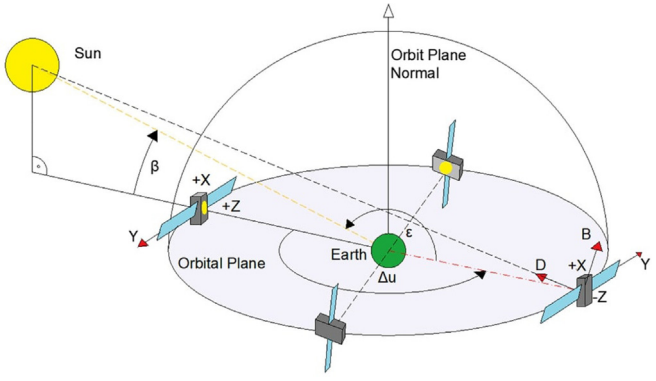

Fig. 8. Sun-satellite-Earth reference frame showing the D, Y, and B directions of the standard ECOM model (Bury et al., 2020).

2.6. Precise orbit determination process

Initially, the satellite orbits of EHI-1 and EHI-2 are estimated using only the GNSS observations. A separate Precise Orbit Determination (POD) process is performed for EHI-1 and EHI-2. The next step involves fixing the carrier phase ambiguities following the single-receiver strategy described by Montenbruck et al. (2018). This algorithm employs the Melbourne-Wübbena (MW) combination and single difference techniques to resolve the wide-lane and narrow-lane ambiguities. With the ambiguities fixed, a subsequent iteration of the POD scheme is performed with the integer ambiguities held constant.

After estimating the orbits and clocks of EHI-1 and −2 using solely GNSS observations, the orbit and clocks of EHI-2 are re-estimated considering both the GNSS and ISL observations. The ISL observations are modelled as a pure range, accounting for all relevant perturbations, while excluding consideration of instrumental biases or clock biases. Hence, these observations are treated as pure ranges with a Gaussian noise. The ISL observations are integrated into the weighted least-squares algorithm as additional observational equations. These laser observations receive higher weighting than GNSS observations due to their presumed higher precision.

During this second estimation, the orbit and clocks of EHI-1 are held fixed to the ambiguity-fixed solution obtained from the GNSS-only POD, while the orbit and clocks of EHI-2 are re-estimated, considering the additional information provided by the ISL observations. Subsequently, the float solution obtained from the GNSS + ISL POD process serves as the input for the integer ambiguity resolution algorithm, enabling the determination of the GNSS + ISL fixed solution for EHI-2. Fig. 9 provides a schematic representation of the two POD processes.

The POD problem is formulated as a reduced-dynamic problem, which is solved using a batch weighted least-squares algorithm. The estimation period is divided into 34-hour arcs, centered on a nominal day. Within each determination arc, various parameters are estimated, including the initial state vector, ECOM-SGRA empirical coefficients, receiver clock biases, and fixed ambiguities per pass. The POD parametrization is presented in Table 6.

To facilitate the presentation of the POD results, the ISL-SGRA frame is introduced. The ISL-SGRA frame is defined based on the baseline between EHI-1 and EHI-2 and the attitude of the spacecraft. In this frame,

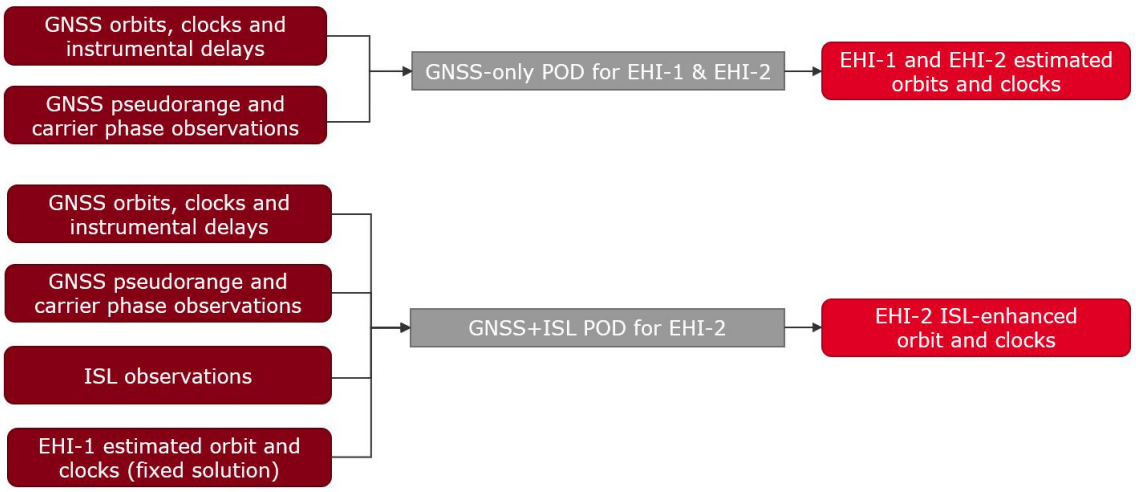

Fig. 9. Diagram of the absolute and relative POD.

the X axis aligns with the ISL direction, pointing from EHI-1 to EHI-2, while the Y axis points towards the black hole Sgr A*. The Z axis is orthogonal to both X and Y. However, it should be noted that this frame is not orthogonal since X and Y are non-orthogonal. This reference frame plays a crucial role in the analysis conducted in this study, providing a consistent coordinate system for various analyses.

The mathematical expressions for ISL-SGRA axes are provided in Eq. (7), and a schematic representation of this coordinate system can be observed in Fig. 10. It is important to clarify that the depicted EHI orbits in Fig. 10 are not an accurate representation of the actual orbits but have been simplified for illustrative purposes.

$$\widehat{\boldsymbol{X}} = \frac{\boldsymbol{r}_2 - \boldsymbol{r}_1}{|\boldsymbol{r}_2 - \boldsymbol{r}_1|}, \widehat{\boldsymbol{Y}} = \frac{\boldsymbol{r}_{SGRA}}{|\boldsymbol{r}_{SGRA}|}, \widehat{\boldsymbol{Z}} = \widehat{\boldsymbol{X}} \times \widehat{\boldsymbol{Y}} \tag{7}$$

3. Results

In order to select an appropriate simulation period, several factors need to be considered. First, it is crucial to ensure that the ISL signal is not blocked by the Earth. Second, the simulation should fully capture the dynamic nature of the problem. Third, the chosen period should be free from eclipses. Lastly, to ensure optimal imagining of the black hole, it is essential to prevent direct solar radiation from interfering with the VLBI signal. Considering these requirements, the selected simulation period is the month of April 2022. The year is selected to maximize the errors in the geopotential.

3.1. Relative orbit estimation results

The accuracy of the relative POD is measured by comparing the estimated relative orbits and the reference relative orbit. In Fig. 11, the results of this comparison throughout the entire month of April 2022 are presented in terms of the three-dimensional position difference. The figure displays the results obtained when all error sources all included for three different scenarios: GNSS-only float, GNSS-only fixed, and GNSS + ISL fixed, where float and fixed refer to the nature of the ambiguity.

Analysing Fig. 11, it can be seen that the fixed solutions display a notably superior performance compared to the float solution, highlighting the importance of integer ambiguity resolution. Within the fixed solutions, the GNSS + ISL POD does not appear to yield a significant improvement in terms of 3D relative position accuracy when compared to the GNSS-only POD. These findings suggest that, at least for the considered accuracy metric, the inclusion of the ISL observations does not provide a substantial advantage over a GNSS-only estimation.

The analysis has identified errors in the geopotential and errors in the GNSS orbits and clocks as the primary sources of error. These errors lead to millimetre-level 3D relative position errors for large baselines. Following them, thermal noise, uncertainties in the instrumental delays and errors in the solar radiation pressure model contribute to sub-millimetre-level 3D relative position errors for large baselines. Lastly, clock biases and laser noise have a negligible effect on the relative orbit accuracy.

To gain further insights into the impact of the ISL observations, it is beneficial to project the previous comparison onto the ISL-SGRA frame. Fig. 12 provides a visual representation of this projection, showcasing the comparison in the three directions of the ISL-SGRA frame for the fixed solutions. It can be observed that the ISL enhances the relative orbit determination in the baseline direction, with differences below 0.1 mm. However, for the other two directions, the ISL does not introduce significant improvements in the determination of the relative distance. Focusing on the Sgr A* direction, both the GNSS-only fixed and GNSS + ISL fixed solutions maintain errors within the range of −10 mm to 10 mm.

Table 6
POD parametrization.

Parameter / Model	Value
Software	
Name and version	FocusPOD
Arc Cut	
Arc lengths	34 h (5 h + 24 h + 5 h)
Handle of manoeuvres	No manoeuvres
Handle of data gaps	No data gaps
Reference System	
Polar motion and UT1	IERS finals2000A.data (Petit and Luzum, 2010)
Pole model	IERS 2010 Conventions (Petit and Luzum, 2010)
Precession/Nutation	IERS 2010 Conventions
Satellite Reference	
Mass and centre of gravity	Fixed as per configuration
Attitude model	Modelled as inertial fixed towards Sag A*
GNSS antenna reference point and orientation	Fixed as per configuration
Gravity	
Gravity field (static)	EIGEN.GRGS.RL04.MEAN-FIELD.quadratic_mean_pole (35x35) (Lemoine et al., 2019)
Gravity field (time-varying)	Drift/annual/semi-annual piece-wise terms (10x10) (Lemoine et al., 2019)
Solid Earth tides	IERS 2010
Ocean tides	FES2014 (35x35) (Lyard et al., 2021)
Atmospheric gravity	Not applied
Atmospheric tides	Not applied
Earth pole tide	IERS 2010
Ocean pole tide	IERS 2010
Third bodies	Sun, Moon, Planets DE405 (Standish, 1998)
Surface Forces and Empiricals	
Radiation pressure model	Empirical ECOM-SGRA model
Earth radiation	Albedo and Infra-red applied
Total Solar Irradiance (TSI)	Not applied
Atmospheric density model	Not applied
Radiation pressure coefficient	Fixed 1 coefficient to 1.0
Drag coefficients	Not applied
ECOM-SGRA empiricals	Estimated 7 sets per arc: D: constant, sin + cos Y: constant, sin + cos B: constant, sin + cos (constrained with 10^{-6} m/s^2, 10^{-9} m/s^2)
GNSS Observations	
Relativity	IERS 2010
Sampling	10 s
Observations	Simulated ionosphere-free linear combinations of phase and pseudo-range observations
Weight	2.7 m (pseudo-range) / 20 mm (carrier-phase)
Signal-to-noise ratio cut-off	30 dB
Down-weighting law	None
Antenna phase-centre wind-up correction	Applied
Antenna phase-centre variation	Applied
GNSS satellite instrumental biases	Simulated
Receiver instrumental biases	Simulated
Thermal noise	Simulated
GNSS Parameters	
Receiver clocks	Estimated per epoch, every 10 s
Receiver ambiguities	Estimated (integer)
GNSS orbits	Perturbed simulated orbits
GNSS clocks	Perturbed simulated clocks
GNSS satellite biases	Perturbed simulated biases
ISL Observations	
Relativity	IERS 2010
Sampling	10 s
Observations	Simulated pseudo-range observations
Weight	1 mm
Noise	1 mm Gaussian noise

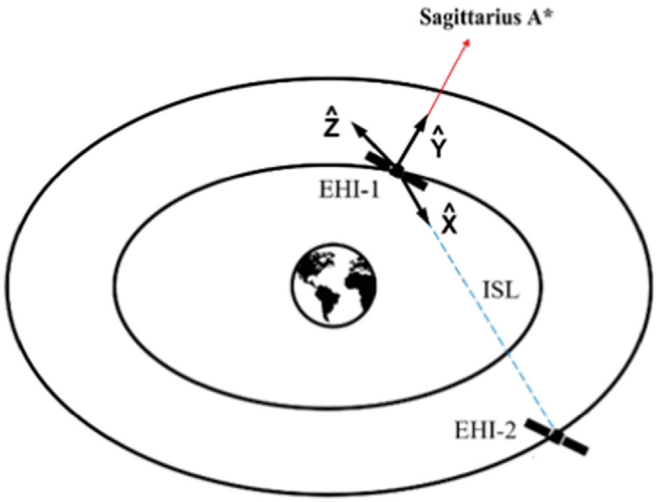

Fig. 10. Representation of the ISL-SGRA frame.

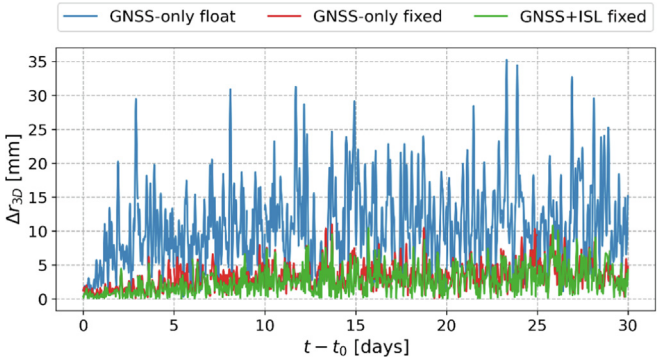

Fig. 11. Comparison between the estimated relative orbit and the reference relative orbit for the month of April 2022.

Table 7 provides a quantitative summary of the statistics of the comparisons, highlighting the root-mean-square (RMS) in the direction of Sgr A*. The results indicate that, in this direction, the RMS and maximum relative position error are slightly lower for the GNSS + ISL fixed solution compared to the GNSS-only fixed solution. Nevertheless, the mean values show the opposite trend. Although not needed for this mission, it is remarkable the extraordinary sub-millimetre level accuracy that is obtained in the baseline projection thanks to the very precise ISL observations.

In addition to the previously discussed observations, it is notable that the error in estimating the relative orbit tends to increase as the distance between the satellites grows. This behaviour can be explained by the fact that when the satellites are close, they experience similar dynamical model errors and they have more GNSS satellites in common view, leading to the cancellation of common errors when computing the relative orbit. However, as the satellites drift apart, they are subject to different dynamical model errors and they have less common visible GNSS satellites, resulting in a reduced cancellation of the shared errors when calculating the relative orbit.

Nevertheless, a larger baseline does not necessarily result in a larger error. There are instances where earlier days exhibit poorer performance compared to later days. This non-linear behaviour arises because the relationship between baseline length and relative dynamical model errors is not solely determined by the size of the baseline. Rather, when the satellites are significantly away from each other, the error behaviour is influenced by how different the specific dynamical perturbation is introduced in each satellite. Similarly, the relationship between baseline distance and the number of GNSS satellites in common view is also non-linear and exhibits a more complex pattern, as shown in Fig. 13.

3.2. Fulfilment of accuracy requirement

The scientific requirements of the mission place particular emphasis on assessing the percentage of observations that meet a specific threshold for relative orbit accuracy. The mission will track the black hole in three frequencies: 3 GHz, 230 GHz, and 557 GHz, with wavelengths of 7, 1.3, 0.54 mm respectively. In principle, it is enough to correlate the VLBI observation with the longest wavelength (7 mm) to allow subsequent VLBI observation correlation with wavelength bootstrapping (Boer & Brinkerink, 2023). To be conservative, the 7 mm is divided by two to obtain a 3D, 3-sigma relative accuracy requirement of 3.5 mm, which is quite challenging. However, it is unclear to the authors whether this requirement can be relaxed in magnitude or sigma, for example requiring only to fulfil the requirement over some period of time, rather than during the whole period of one month.

Considering this ambitious requirement, Fig. 14 displays the percentiles for the GNSS + ISL fixed solution. For this solution, the 3-sigma value in the direction of Sgr A* is 8.29 mm, and only 86.3% of the observations meet the 3.5 mm relative navigation requirement in this direction, falling significantly short of the desired 99.7% goal. Similar results were found for the GNSS-only fixed solution but with 3-sigma equal to 8.70 mm and 82.7% of the observations meeting the 3.5 mm goal.

3.3. Analysis of empirical accelerations

In the context of this problem, there are two potential approaches to incorporate empirical accelerations into the dynamical model. The first method involves the use of Cycle-Per-Revolution (CPR) accelerations, which are generally applied in the along-track and cross-track directions. The second approach involves the introduction of ECOM-SGRA accelerations, which are specifically defined within the ECOM-SGRA frame. To optimize the absorption of dynamical model errors, it is necessary to carefully analyse how to combine these accelerations and determine which ones should be incorporated, as well as the optimal quantity to be introduced.

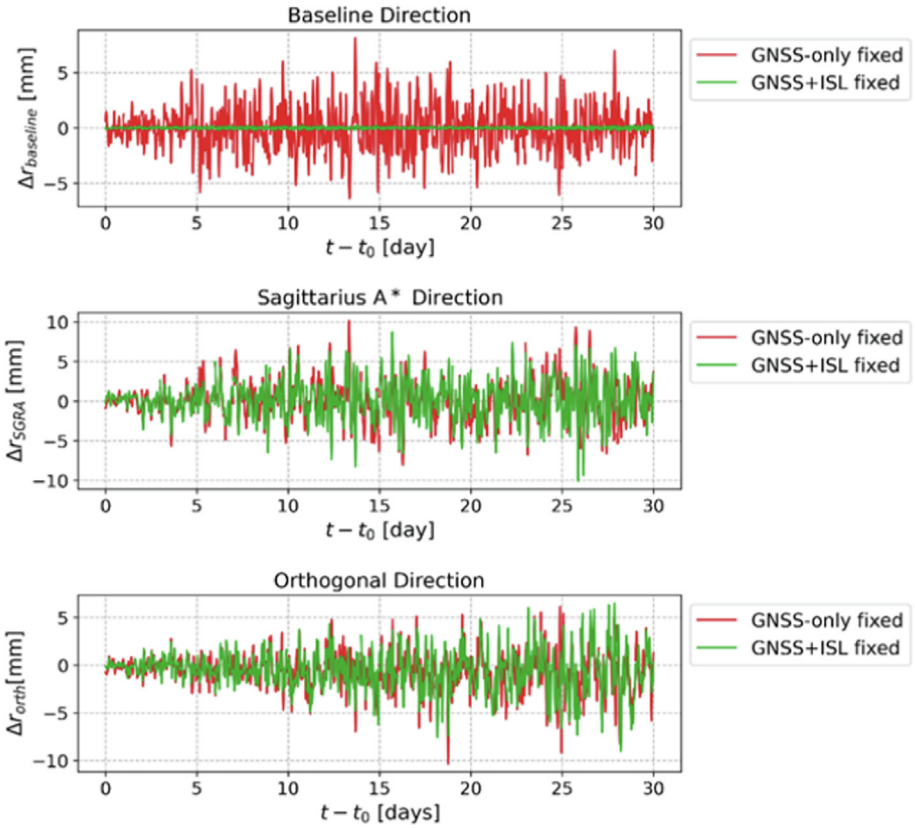

Fig. 12. Comparison between the estimated relative orbit and the reference relative orbit projected in the ISL-SGRA frame for the month of April 2022.

Table 7
Summary of the comparison statistics between the estimated relative orbit and the reference relative orbit for the month of April 2022. The RMS in the direction of Sgr A* is highlighted in red.

Solution	Stat.	Base.	SgrA*	Orth.	3D
GNSS-only float	Mean [mm]	−0.42	−0.88	−1.42	10.93
	RMS [mm]	6.57	7.43	6.83	12.39
	Max [mm]	22.27	24.21	26.54	35.25
GNSS-only fixed	Mean [mm]	−0.01	0.05	−0.63	3.44
	RMS [mm]	1.99	2.59	2.13	3.91
	Max [mm]	8.12	10.15	6.14	10.98
GNSS + ISL fixed	Mean [mm]	−0.004	0.12	−0.56	2.76
	RMS [mm]	0.076	2.38	2.08	3.33
	Max [mm]	0.250	8.71	6.49	10.81

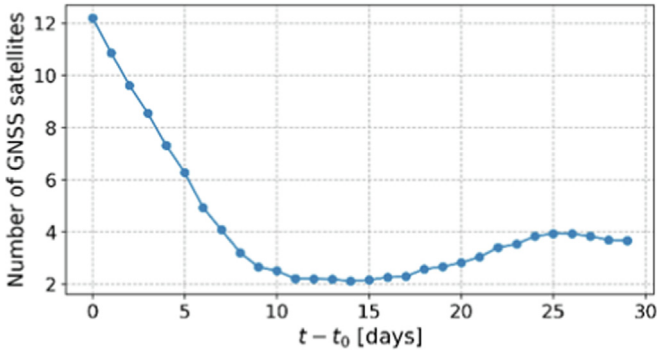

Fig. 13. Mean number of GNSS satellites in common view per day during the month of April 2022.

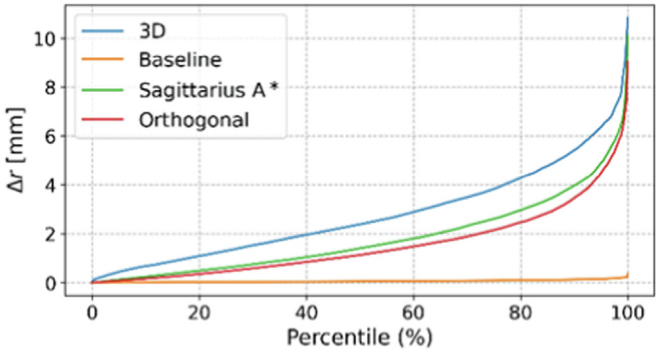

Fig. 14. Percentiles of the relative position errors for the GNSS + ISL fixed solution during the month of April 2022.

It was determined that the most effective approach was to exclusively employ the 9 ECOM-SGRA coefficients without incorporating any CPRs. This method allowed the ECOM-SGRA coefficients to absorb, in addition to SRP model errors, also the errors typically handled by CPRs, such as those arising from geopotential model errors. Estimating both the ECOM-SGRA coefficients and the CPRs did not yield any advantages and only increased the computational time. The optimal setup involved using 34-hour estimation arcs with 7 sub-intervals, which corresponds to approximately one sub-interval per orbit revolution since the orbital period is about 5 h.

Fig. 15 provides an overview of the estimated ECOM-SGRA coefficients for EHI-1 throughout the entire month of April, specifically for the GNSS + ISL fixed solution. Similar coefficient patterns were observed for EHI-2. In this figure, it can be observed that the constant coefficients are two or three orders of magnitude larger than the sinusoidal coefficients and present a smooth increasing evolution. As expected, D_0 is the largest coefficient because it represents the direction pointing towards the Sun, and therefore, it absorbs a significant portion of the SRP effect. Although the cosine/sine terms are relatively small, their estimation contributes significantly to the results and should not be disregarded.

3.4. Sensitivity to errors in the GNSS orbits and clocks

The errors introduced in the GNSS orbits and clocks during the POD have been identified as one of the dominant sources of error in this study, resulting in millimetre level 3D relative position errors for large baselines. Thus, a sensitivity analysis is conducted to further evaluate the impact of these errors on the relative orbit accuracy.

In this sensitivity analysis, the impact of different values of the sinusoidal orbit error amplitude (σ_A) and the standard deviation of the Gauss–Markov clock errors (σ_w) is studied. The correlation time (τ) of the Gauss–Markov clock errors remains fixed at its nominal value for the sake of simplicity. For this analysis, the values of σ_A and σ_w are modified by 25%, 50%, 75%, and 125% from their nominal values. The nominal values of these variables can be found in Section 2.

In Fig. 16, the 3-sigma values of the 3D error and the error projected in the ISL-SGRA frame are presented for all five scenarios alongside the requirement threshold. The results exhibit a relatively linear relationship, where increasing errors in the GNSS products corresponds to higher 3-sigma values of the relative orbit error. Fig. 15 indicates that only the '25%NOMINAL' scenario, where the nominal errors are reduced by 75%, satisfies the requirement 3 $\sigma_{SGRA} < 3.5$ mm. Nevertheless, based on the observed linear trend in Fig. 16, it can be inferred that the requirement could be met if errors are lower than 40% of the nominal errors. These 40% nominal errors correspond to a standard deviation of 8 mm for harmonic orbit

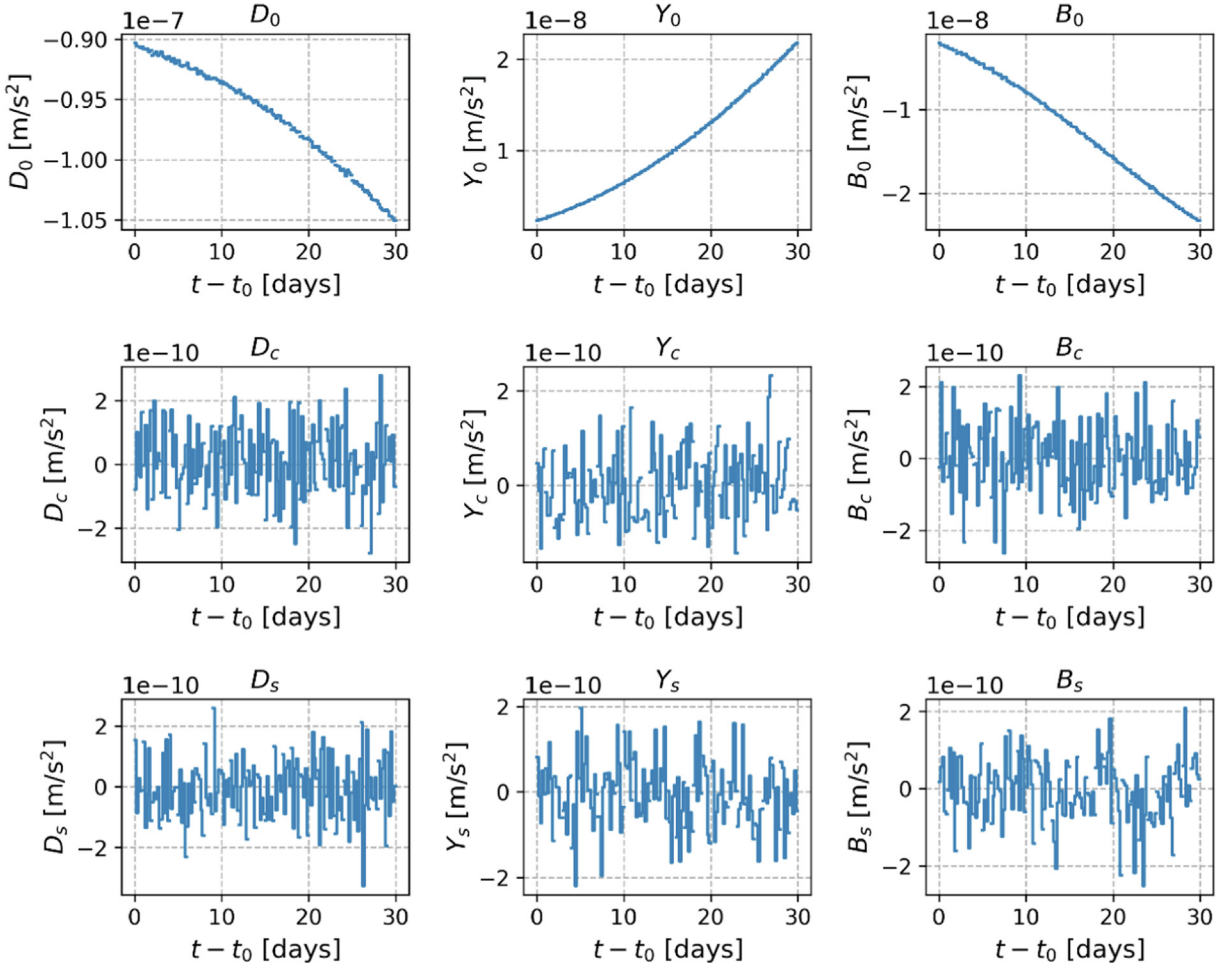

Fig. 15. Evolution of the ECOM-SGRA coefficients for EHI-1 for April 2022, corresponding to the GNSS + ISL fixed solution.

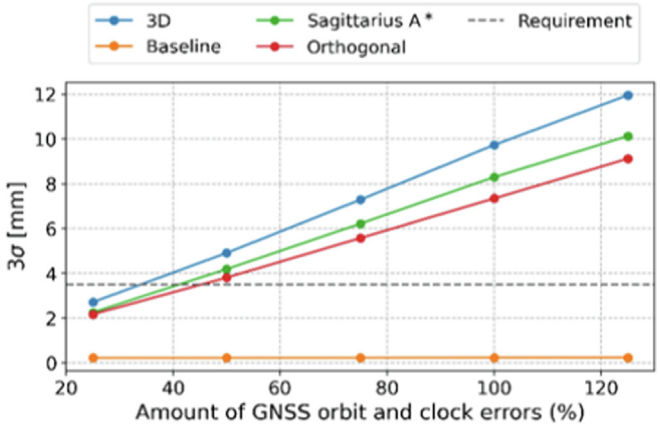

Fig. 16. Sensitivity analysis of 3-sigma values for the GNSS + ISL fixed solution for different scenarios with varying GNSS orbit and clock errors. The requirement of 3.5 mm is illustrated with a dashed line.

errors and a standard deviation of 28 ps for Gauss–Markov clock errors.

4. Conclusions and future work

4.1. Conclusions

One of the key findings of this study is the crucial role of integer ambiguity resolution in achieving the demanding relative navigation requirements of the mission. It was determined that fixing the ambiguities to an integer value leads to a significant enhancement in the accuracy of the relative orbit determination. This improvement is evident not only in the overall evolution of the three-dimensional relative position error but also when examining its projection along the Sgr A* direction.

In terms of employing the Intersatellite Link (ISL) for improving relative orbit accuracy, the analysis revealed that the ISL primarily contributed to a more precise estimation of the baseline in the direction corresponding to the ISL observations. In this specific direction, the root-mean-square (RMS) of the comparison between the estimated relative orbit and the reference relative orbit was below 0.1 mm, while it exceeded 1 mm when relying solely on GNSS observations. Although the exceptional accuracies achieved in this direction may not be necessary for the EHI mission, they hold great promise for other mission scenarios where this direction plays a prominent role.

However, when examining the baseline projection along the Sgr A* direction, the introduction of the ISL observations resulted in only a modest enhancement. The performance improvement in this critical direction was observed to be relatively minor, with an approximate 8% improvement in the RMS and a 5% improvement in the 3-sigma variables when compared to the results obtained using GNSS observations alone. Despite this, it is worth noting that the achieved relative accuracy in this direction remains relatively accurate, consistently below the 1 cm level for all possible baseline distances.

The relative position errors escalate as the satellites progressively separate from each other. For this reason, the objective of attaining a 3-dimensional relative position accuracy of 3.5 mm (3-sigma) along the Sgr A* direction is not met. The obtained 3-sigma value exceeds 8 mm, and an 86.3% of the observations meet this requirement, falling short of the desired 99.7% threshold. However, it is unclear whether a 3-sigma over one month is really needed by the mission. Achieving the original requirement necessitates exceptionally precise GNSS orbits and clocks. Only by reducing the nominal considered errors by more than 60% was it feasible to meet the relative navigation requirement.

Lastly, it is important to highlight that the proposed modified ECOM empirical model, known as ECOM-SGRA, which considers the specific attitude law of the EHI satellites, proved to be highly effective in capturing the influence of solar radiation pressure modelling uncertainties, as well as other dynamic model errors. Therefore, it was observed that no additional empirical accelerations, such as CPR accelerations, need to be introduced as the ECOM-SGRA model already absorbs the effects typically accounted for by CPRs.

4.2. Future work

Throughout this study, certain assumptions were made regarding the simulation of the GNSS and ISL observations, which may need reconsideration in future research. Firstly, the current ISL noise model relies on a simplistic Gaussian noise assumption, which may not fully capture the complexities of the link. It would be advisable to incorporate a more complex noise model that takes into account the characteristics of the optical instrument and factors such as the baseline distance. Secondly, the simulation could be improved by considering the coupling between the GNSS clocks and the instrumental biases, as well as the intersystem bias between GPS and Galileo. Thirdly, the ECOM-SGRA model should be revisited if the attitude law of the EHI satellites is modified. Lastly, if a more sophisticated attitude law is implemented, leading to the rotation of the solar panels or the satellite body, the impact of multipath effects should be investigated.

In addition to the previous considerations, other alternative approaches can be explored to enhance the accuracy of baseline determination in the direction of the black hole. One possibility would be to incorporate additional GNSS constellations, such as BeiDou or QZSS (Quasi-Zenith Satellite System) and assure that the GNSS tracking channel selection system favours satellites in common view. Considering that most of the GNSS observations will be free from ionosphere delay could be considered to investigate the use of a raw processing. Another approach worth investigating is a network processing scheme, where the orbits and clocks of both GNSS satellites and receivers

are simultaneously estimated. A network approach has the potential to mitigate the impact of errors in the GNSS products, especially the effect of instrumental delays. Finally, exploring the potential synergies between the ground-based VLBI telescopes of the EHT network and the EHI mission presents an intriguing opportunity.

Declaration of competing interest

The authors declare that they have no known competing financial interests or personal relationships that could have appeared to influence the work reported in this paper.

Acknowledgements

The authors acknowledge ESA for the original idea of this mission. The provision of GNSS orbit, clock, and biases products by the CODE and GFZ, and GNSS data and products of Sentinels by the CPOD Service is also greatly appreciated.

References

Akiyama, K., Alberdi, A., Alef, W., et al., 2019. First M87 event horizon telescope results. I. The shadow of the supermassive black hole. Astrophys. J. Lett. 875 L1. https://doi.org/10.3847/2041-8213/ab0ec7.

Alawieh, M., Hadaschik, N., Franke, N., & Mutschler, C. (2016). Inter-Satellite Ranging in the Low Earth Orbit. Presentation at 10th International Symposium on Communication Systems, Networks and Digital Signal Processing, Prague, Czech Republic. 2016, pp. 1-6. https://doi.org/10.1109/CSNDSP.2016.7573920.

Amaro-Seoane, P., Audley, H., Babak, S., et al. (2019). Laser Interferometer Space Antenna: LISA. Albert Einstein Institute. Hannover. https://doi.org/10.48550/arXiv.1702.00786.

Arnold, D., Meindl, M., Beutler, G., et al., 2015. CODE's new solar radiation pressure model for GNSS orbit determination. J. Geod. 89, 775–791. https://doi.org/10.1007/s00190-015-0814-4.

Berzosa, J., Fernández Martín, C., Matuszak, M., et al. (2023). Reprocessing of Copernicus Sentinel POD solutions with COST-G geopotential models, Presentation at *EGU General Assembly 2023*, Vienna, Austria. https://doi.org/10.5194/egusphere-egu23-16137.

Boer, K. L., & Brinkerink C. (2023). Multi-Wavelength Image Processing for Space-to-Space VLBI. Final presentation for ESA project. https://navisp.esa.int/uploads/files/documents/Radboud%20University_%20Multi%20Wavelength%20Study.pdf.

Bury, G., Sosnica, K., Zajdel, R., Strgugarek, D., 2020. Toward the 1-cm Galileo orbits: challenges in modeling of perturbing forces. J. Geod. 94 (16). https://doi.org/10.1007/s00190-020-01342-2.

Fernández Martín, C., Berzosa Molina, J., Bao Cheng, L., et al. (2023). FocusPOD, the new POD SW used at CPOD Service, Presentation at EGU General Assembly 2023, Vienna, Austria. https://doi.org/10.5194/egusphere-egu23-1908.

Galleani, L., Sacerdote, L., Tavella, P., Zucca, C., 2003. A mathematical model for the atomic clock error. Metrologia 40 (3), S257. https://doi.org/10.1088/0026-1394/40/3/305.

Giorgi, G., Kroese, B., & Michalak, G. (2019). Future GNSS constellations with optical inter-satellite links. Preliminary space segment analyses. Presentation at 2019 IEEE Aerospace Conference, 1–13, Big Sky, MT, USA. https://doi.org/10.1109/AERO.2019.8742105.

GMV. (2022). PRP-MEO: Final Report (tech. rep. NAVISP1-TN-GMV-024-17).

Jäggi, A., Meyer, U., Lasser, M., et al., 2020. International Combination Service for Time-Variable Gravity Fields (COST-G) - Start of Operational Phase and Future Perspectives. In: Freymueller, J.T., Sánchez, L. (Eds.), Beyond 100: the next Century in Geodesy" IAG Symposia Series 152. Springer, Cham. https://doi.org/10.1007/1345_2020_109.

Kaplan, E., Hegarty, C., 2006. Understanding GPS principles and applications. Artech House Publishers, London.

Kornfeld, R., Arnold, B., Gross, M., et al., 2019. GRACE-FO: The gravity recovery and climate experiment follow-on mission. J. Spacecr. Rocket. 56, 931–951. https://doi.org/10.2514/1.A34326.

Kudriashov, V., Martin-Neira, M., Roelofs, F., et al., 2021. An Event Horizon Imager (EHI) Mission Concept Utilizing Medium Earth Orbit Sub-mm Interferometry. Chinese J. Space Sci. 41 (2), 211. https://doi.org/10.11728/cjss2021.02.211.

Lemoine, J.M., Biancale, R., Reinquin, F., Bourgogne, S., Gégout, P.. CNES/GRGS RL04 Earth gravity field models, from GRACE and SLR data. https://doi.org/10.5880/ICGEM.2019.010.

Lyard, F.H., Allain, D.J., Cancet, M., Carrère, L., Picot, N., 2021. FES2014 global ocean tides atlas: design and performance. Ocean Sci. 17, 615–649. https://doi.org/10.5194/os-17-615-2021.

Loscher, A. (2010). Atmospheric influence on a laser beam observed on the OICETS – ARTEMIS communication demonstration link. *Atmospheric Measuring Techniques*, 3, 1233–1239. https://doi.org/10.5194/amt-3-1233-2010.

Michalak, G., Neumayer, K. H., & König, R. (2020). Precise Orbit Determination of the Kepler Navigation System - a Simulation Study. Presentation at 2020 European Navigation Conference (ENC), 1–10, Dresden, Germany. https://doi.org/10.23919/ENC48637.2020.9317467.

Michalak, G., Glaser, S., Neumayer, K., König, R., 2021. Precise orbit and Earth parameter determination supported by LEO satellites, inter-satellite links and synchronized clocks of a future GNSS. Adv. Space Res. 68 (12), 4753–4782. https://doi.org/10.1016/j.asr.2021.03.008.

Montenbruck, O., & Gill, E. (2000). *Satellite Orbits: Models, Methods and Applications.* Springer Berlin, Heidelberg. https://doi.org/10.1007/978-3-642-58351-3.

Montenbruck, O., Hackel, S., Jäggi, A., 2018. Precise orbit determination of the Sentinel-3A altimetry satellite using ambiguity-fixed GPS carrier phase observations. J. Geod. 92, 711–726. https://doi.org/10.1007/s00190-017-1090-2.

Olynik, M., Petovello, M., Cannon, M., Lachapelle, G., 2002. Temporal impact of selected GPS errors on point positioning. GPS Solut. 6, 47–57. https://doi.org/10.1007/s10291-002-0011-9.

Perello-Gisbert, J., & Garcia, A. (2010). GNSS navigation on the Moon (tech. rep. TEC ETN/2010.110/JVPG). European Space Agency.

Petit, G., & Luzum, B. (2010). *IERS Conventions (2010)*. Verlag des Bundesamts für Kartographie und Geodäsie (Publishing house of the Federal Office for Cartography and Geodesy), Frankfurt.

Prange, L., Orliac, E., Dach, R., Arnold, D., Beutler, G., Schaer, S., Jäggi, A., 2017. CODE's five-system orbit and clock solution—the challenges of multi-GNSS data analysis. J. Geod. 91, 345–360. https://doi.org/10.1007/s00190-016-0968-8.

Prange, L., Beutler, G., Dach, R., Arnold, D., Schaer, S., Jäggi, A., 2020. An empirical solar radiation pressure model for satellites moving in the orbit-normal mode. Adv. Space Res. 65 (1), 235–250. https://doi.org/10.1016/j.asr.2019.07.031.

Senior, K., Ray, J., Beard, R., 2008. Characterization of periodic variations in the GPS satellite clocks. GPS Solut. 12, 211–225. https://doi.org/10.1007/s10291-008-0089-9.

Standish, E.M. (1998). JPL Planetary and Lunar Ephemerides, DE405/LE405. JPL IOM 312.F-98-048.

Teunissen, P., & Montenbruck, O. (2017). *Springer Handbook of Global Navigation Satellite Systems.* Springer, Cham. https://doi.org/10.1007/978-3-319-42928-1.

Urschl, C., Beutler, G., Gurtner, W., Hugentobler, U., Schaer, S., 2007. Contribution of SLR tracking data to GNSS orbit determination. Adv. Space Res. 39 (10), 1515–1523. https://doi.org/10.1016/j.asr.2007.01.038.

Zangerl, F. (2017). PODRIX: Performance Analysis (tech. rep. P-11284-ANA-0022-RSA). RUAG Space.
Zhu, J., Li, H., Li, J., Ruan, R., Zhai, M., 2022. Performance of dual one-way measurements and precise orbit determination for BDS via inter-satellite link. Open Astron. 31, 276–286. https://doi.org/10.1515/astro-2022-0034.